

Application of hydrodynamic lubrication in discrete element method (DEM) simulations of wet bead milling chambers



Ramon Cabisco^{a,*}, Tom Jansen^a, Michele Marigo^a, Christopher Ness^b

^a Johnson Matthey Technology Centre, P.O. Box 1, Belasis Avenue, Billingham, Cleveland TS23 1LB, UK

^b School of Engineering, University of Edinburgh, Edinburgh EH9 3JL, UK

ARTICLE INFO

Article history:

Received 30 November 2020

Received in revised form 29 January 2021

Accepted 30 January 2021

Available online 18 February 2021

ABSTRACT

Fine grinding in wet stirred media mills is a key operation in numerous industrial processes. During wet milling, grinding beads (typically millimetre scale) collide with each other under rapid agitation. These collisions transfer energy into the surrounding medium, a feed stream comprising a premixed slurry (a suspension of micron-sized particles), leading to a reduced particle size. Numerical simulation provides an opportunity to gain mechanistic insight by modelling the influences of grinding media, agitator speed and slurry rheology on the breakage. The multiphase nature of wet milling necessitates models that account for both the solid grinding beads and the slurry feed. Established fluid-particle coupled methods are in principle capable of doing this, but the need to resolve the large hydrodynamic lubrication forces between near-contacting beads demands extremely high fluid field resolution, leading to proliferating simulation size and cost. To address this challenge, a Discrete Element Method (DEM) simulation for a lab scale mill is presented in which the bead-bead interaction includes pairwise hydrodynamic lubrication in addition to frictional contact forces. The model accounts for multiphase effects in a simplified yet physically well-motivated way, circumventing the computational cost of a fully fluid-resolved model. A systematic model calibration against the laboratory mill is presented, and thereafter the model provides a good estimation for the empirical power draw across the full range of rotation speeds and considered feed viscosities. The differences in energy dissipation modes and the local distribution of collisions along the mill chamber are examined for the extreme viscosity condition, revealing that most energy dissipation is due to inter-particle forces acting tangentially (shearing and rolling) while highly energetic collisions (impact and torsion), relying on free flows and inter-bead mobility, are relatively unimportant.

© 2021 Elsevier B.V. All rights reserved.

1. Introduction

Agitated wet media milling, often referred to as stirred media milling, is a key operation employed in manufacturing industries (pharmaceuticals, coatings, catalysts, among others) to reduce the size of suspended particles in a wide range of inorganic and organic products [1]. The basic setup includes a stationary chamber partially filled with grinding media (typically millimetre-scale beads) which are propelled by an agitator or *stirrer*. Collisions between grinding media dissipate energy into the product stream, leading to breakage of suspended particles. Mill designs include horizontal and vertical types and, depending on the technology, they can operate either with dry or wet feeds [2]. Typically, wet processing is advantageous because the liquid phase maximises the mobility within the chamber and provides a means to transport the fines out of the mill [3]. The early work of Rumpf defined two general stress types in mills [4]: compression/slow impact leading to abrasion and cleavage due to shear and compression stresses

(velocity $< 20 \text{ m} \cdot \text{s}^{-1}$) and fast impact producing fracture (velocity $> 20 \text{ m} \cdot \text{s}^{-1}$). Particle size fragmentation in horizontal stirred mills typically proceeds by shearing mechanisms. Although the energy transfer efficiency of stirred mills is in some cases questioned [5], they remain widely used, in particular for ultra-fine grinding (below $10 \mu\text{m}$) [3].

A host of lab-scale studies have been conducted to elucidate the effect of mill design and operation conditions on the breakage rate and fragment size of the output slurry [6,7]. The movement and collision of the grinding media is of paramount interest, helping set the energy transfer to the product and the residence time. Both quantities may be measured experimentally by introducing solid and liquid tracers to investigate slurry transport and particle breakage [5,8,9]. In parallel to experimental methods, Discrete Element Method (DEM) simulations have been employed to track grinding media trajectories and collisions, and to evaluate the charge behaviour, torque and power draw for *dry* mills with different designs and at different scales [10,11]. Common outputs of such simulations are the stress energy distribution, the number of grinding media contacts per time unit, and the spatial distribution of the media within the simulation domain [3,12]. With few exceptions, the presence of feed/product particles is not considered in simulations

* Corresponding author.

E-mail address: ramoncabisco.martinoli@matthey.com (R. Cabisco).

due to their extremely high number even before breakage [13]. This presents a limit for DEM as the simulation time is linearly (at best) related to the number of particles in the system [14]. Restricting the analysis to the flow, motion and residence time of the grinding media nonetheless constitutes a valid and useful approach to evaluating the effect of processing conditions, contributing to the definition of milling good practices and optimisation.

For wet operated mills, the effect of fluid has been considered by coupling DEM simulations with an additional numerical method, such as particle finite element method (PFEM) [15], computational fluid dynamics (CFD) [16] or smoothed particle hydrodynamics (SPH) [17]. CFD is a grid-based Eulerian method based on continuum mechanics and control volume methods and is computationally efficient for single phase flows. In practice, a DEM-CFD coupling for milling applications presents some challenges, as it involves complex geometries and free surface flows, restricting the analysis to a small representative section or adding cost to simulations. For instance, in the Volume of Fluid (VOF) CFD method, the physical domain has to be continuously remeshed, even if the volume is not occupied by fluid [18]. Alternatively, in SPH, the fluid is represented by particles with an associated mass, volume, viscosity, pressure and position, removing the need to mesh the system [19]. A challenge associated with the standard SPH formulation has been the development of robust and rigorous definition of boundary conditions and turbulence, among other issues [20]. Regardless of the precise approach to modelling the fluid phase, however, highly packed systems such milling chambers charged with grinding media require very fine resolution (at least an order of magnitude smaller than the grinding media, leading to at least three orders of magnitude more computations in three dimensions) to properly capture the flow in the interstices between beads. It is essential to capture the fluid behaviour in these narrow gaps as this is precisely where the breakage occurs, so it will be crucial for determining the overall flow field in the chamber. Coupled approaches in which the grinding media is captured with DEM and the slurry is treated as a single-phase fluid are naturally an improvement over models that omit the fluid phase entirely, but the computational intractability of properly resolving thin films between beads limits what can be achieved in a practicable simulation time.

Instead, a compromise between computational efficiency and accurate fluid description might be achieved by replacing the continuum description of the fluid phase with a pairwise hydrodynamic lubrication model in the DEM representation of the milling beads. Such a model would retain the DEM approach to simulating the grinding media, and would incorporate the fluid – that is, the slurry containing the feed/product particles – simply as an additional pairwise particle-particle interaction term, thus negating the need for one of the coupled approaches described above. There is a growing body of literature demonstrating that such an approach is appropriate for making computational predictions of the complex rheology of dense suspensions of solid non-Brownian particles under rheometric flows [21–25]. Such materials exhibit a complex rheology, as the viscosity is related to the solid volume fraction, the shear rate and the stress history of the particles [21]. This rheology can be characterised analogously to dry granular materials at low Reynolds numbers and has been successfully predicted by DEM simulations enhanced with lubrication forces by several authors, under controlled flow conditions of shear, extensional and transient flow [22–24,26,27].

The present study provides a proof-of-concept for the applicability of a DEM model with hydrodynamic lubrication forces for simulating a wet mill setup. Since the evolving rheology of milled slurry is itself a highly challenging topic [28], the present work treats the slurry as a single-phase fluid of constant (i.e. independent of the rate and the milling history) viscosity, in both experiment and simulation. Although this is a rather simplified approach, such a step is essential as an entry point to particle-based simulation of wet milling. New fundamental understanding of the constitutive behaviour of the slurry, a task requiring

further experimental and theoretical developments, can be input to the modelling framework presented here to achieve, in future, a holistic model for wet milling [28,29]. Proceeding with the simplified model, collision energies and velocities of the grinding media for an agitated mill are presented under various conditions. As a reference setup, a series of binary mixtures of water and glycerol with no processed material (to retain the constant viscosity conditions of the simulation) are input to a Netzsch Labstar LS1 mill to determine the power draw for a given set of rotation speeds and viscosities. A milling chamber of equivalent dimensions and filling charge is simulated. First, a calibration procedure for the Coulombic friction coefficient (μ_p) of the grinding beads and the liquid viscosity parameter ($\eta_{f,i}$) is carried out. μ_p is systematically varied in simulations of dry grinding media to find the best match between the simulated and the experimental power draw. Once a best-fitting μ_p value is determined, η_f is obtained for each binary mixture following an analogous comparison with the experimental power draw. Next, a critical examination of the effects of η_f on the flow and the underlying energy dissipation mechanisms (impact, shearing, rolling and torsion) along the mill vessel is provided. Finally, the computational performance of the reported simulations is examined in order to highlight the substantial time benefit of the modelling strategy presented here in comparison to other methodologies.

2. Experimental method for model calibration and validation

Experimental tests were performed on a Labstar LS1 horizontal laboratory stirred media mill (NETZSCH-Feinmahltechnik GmbH, Germany) (Fig. 1) with an empty volume of 0.66 l. Experiments were carried out with constant recirculation of the liquid mixture (described below) through the milling chamber from an agitated tank and the contents of the milling chamber were refrigerated by a cooling jacket supplied with chilled water at 5 °C, keeping the temperature of the process liquid in the range 15–25 °C. More details about the instrumentation are given elsewhere [30].

Near-spherical zirconium silicate (ZrSiO_4) beads of diameter 1.8 mm with a very low roughness and high sphericity (FOX Industries, USA) were used as the grinding agent [31]. ZrSiO_4 exhibits a hard-brITTLE behaviour and it is assumed to be a fully rigid body. A total charge of beads of 2176 g, corresponding to approximately 130,000 units and a solid filling volume of the grinding chamber of 43% was used in all tests. No product is processed, instead a premixed mother liquor composed of binary mixtures of demineralised water and glycerol at different composition was chosen to evaluate the effect of slurries with constant viscosity, consistent with our simplified simulation approach.

Table 1 summarises the experimental tests reported. For each case, the mill rotation speed is ramped up from 1000 to 4000 rpm at 500 rpm intervals, pausing at each interval for around 30 s (the system is found to reach steady state within this time period) to record a steady value of the stationary power draw (P_{stat}) (see Experiments 1 to 5, in which the viscosity is sequentially increased). The speed intervals are chosen to reflect the typical operating conditions of the lab mill. The experimental net power input (P_i) is given by

$$P_i = P_{\text{stat}} - P_0 \quad (1)$$

Where P_0 is the no-load or idle power consumption, accounting for the power lost to friction inside the bearings and the seal at a given rotational speed. P_0 is obtained operating the mill without grinding media and liquid (Experiment 0).

The liquid mixture, a “constant viscosity slurry”, is driven by a peristaltic pump operating at a very low rotation frequency (14 rpm), giving a total throughput of 0.140 l/min. Water/glycerol mixtures exhibit a viscosity that is insensitive to shear rate, but highly sensitive to temperature. The temperature is recorded at every P_{stat} acquisition. Dynamic viscosity values ($\eta_{f,\text{exp}}$) for water/glycerol mixtures are corrected with

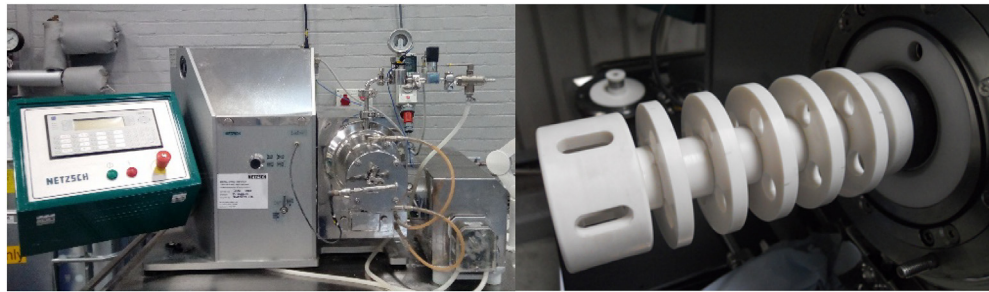


Fig. 1. (Left) Netzsch Labstar LS1 mill. (Right) Ceramic perforated disk.

a four-parameter correlation [32,33]. Plots of the power consumption as a function of the rotation frequency for each of Experiments 0–5 are presented later in Fig. 7.

3. Discrete element method (DEM)

3.1. Contact model with lubrication forces

DEM simulations are carried out using a modified version of LIGGGHTS (based on LIGGGHTS v3.2.0, DCS Computing GmbH, Austria) [34], which computes the grinding bead trajectories and interactions within the milling chamber [35]. The positions, velocities, and interaction forces of all beads are explicitly determined over time and are updated according to Newton's second law. Bead-bead contact forces comprise solid and fluid contributions, summarised in Fig. 2. The former are conventional granular-type contacts used in DEM, whereas the latter represent our novel approach to representing the fluid phase with pairwise hydrodynamic lubrication forces. Beads i and j interact when they are in contact through a repulsive force with normal and tangential components given by a linear spring-dashpot model for stiffness constants k_n and k_t (related to the Young's modulus and Poisson's ratio of the material), normal damping coefficient γ_d , centre-to-centre displacement δ_{ij} , normal component of the relative velocity of the two spheres v_{ij} and elastic shear displacement u_{ij}^t ,

$$F_{ij}^{c,n} = k_n \delta_{ij} n_{ij} - \gamma_d v_{ij} \quad (2)$$

$$F_{ij}^{c,t} = -k_t u_{ij}^t - \gamma_d v_{ij} \quad (3)$$

The bead-wall interactions are analogously determined by Eq. 2 and 3. Following common numerical practice, the stiffnesses are reduced in comparison to the experimental system by a factor of $\sim 10^4$, leading to a substantial speed-up [36,37]. In DEM the time step adopted for a particle interaction is inversely proportional to the square root of Young's modulus. Thus, decreasing the Young's modulus allows the time step in the numerical integration to be increased, so the total computation time can be reduced. It is demonstrated in a previous article [22] that this procedure does not affect the bulk stresses for the particle interaction model used here. A Coulomb friction coefficient μ_p limits the tangential force to

$$| F_{ij}^{c,t} | \leq \mu_p | F_{ij}^{c,n} | \quad (4)$$

μ_p will be calibrated based on experimental data below. Since the hydrodynamic lubrication forces described below operate in the viscous limit, the specified damping parameter for the bead-bead contact has minimal effect on the results, and dissipation is governed largely by the fluid forces described in the following. We choose a restitution coefficient of 0.5 to be consistent with the literature [38]. Given the high bead loading, it is assumed, following insights from previous work [39], that the main contribution to the overall stresses is that arising from direct bead-bead contacts, as opposed to bead-fluid interactions. Moreover, and considering the high bead loading, it is assumed that stress transmission in the fluid is predominantly mediated by thin films separating near-contacting beads, as opposed to by long-range hydrodynamics. This effect is modelled by including in the contact model pairwise hydrodynamic lubrication forces with normal and tangential forces given by [22].

$$F_i^{l,n} = \eta_{f,i} \left[\left[X_{11}^A n_{ij} \otimes n_{ij} + Y_{11}^A (I - n_{ij} \otimes n_{ij}) \right] (v_i - v_j) + Y_{11}^B (\omega_1 \times n_{ij}) + Y_{21}^B (\omega_2 \times n_{ij}) \right] \quad (5)$$

$$F_i^{l,t} = \eta_{f,i} \left[Y_{11}^B (v_i - v_j) \times n_{ij} - (I - n_{ij} \otimes n_{ij}) [Y_{11}^C \omega_1 + Y_{12}^C \omega_2] \right] \quad (6)$$

Where $\eta_{f,i}$ is the fluid viscosity, v_i and v_j are the velocity vectors, n_{ij} is the centre-to centre unit vector pointing from particle j to i , and I is the identity matrix. Operators \otimes and \times account for the outer product (Hadamard product) and the cross product, respectively. X_{11}^A , Y_{11}^A , Y_{21}^B , Y_{11}^C and Y_{12}^C are scalar resistances that comprise short range contributions defined by

$$X_{11}^A = 6\pi r_i \left[\frac{2\beta^2}{(1+\beta)^3} \frac{1}{\xi} + \frac{\beta(1+7\beta+\beta^2)}{5(1+\beta)^3} \ln\left(\frac{1}{\xi}\right) \right] \quad (7)$$

$$Y_{11}^A = 6\pi r_i \left[\frac{4\beta(1+7\beta+\beta^2)}{15(1+\beta)^3} \ln\left(\frac{1}{\xi}\right) \right] \quad (8)$$

$$Y_{21}^B = -4\pi r_j^2 \left[\frac{\beta^{-1}(4+\beta^{-1})}{5(1+\beta^{-1})^2} \ln\left(\frac{1}{\xi}\right) \right] \quad (9)$$

Table 1

Summary of experimental tests carried out at the Netzsch Labstar mill LS1.

Experiment	Grinding agent	Processed liquid mixture	Operation
0	None	None	Idle power (P_0) acquisition
1			Stationary power (P_{stat}) acquisition
2		100% water (v/v)	
3	Media: 1.8 mm ZrSiO ₄ beads	35% water + 65% glycerol (v/v)	Power acquisition (P_{stat}). Mother liquor pumped at 14 rpm
4	Dry mass: 2176 g	15% water + 85% glycerol (v/v)	
5		5% water + 95% glycerol (v/v)	

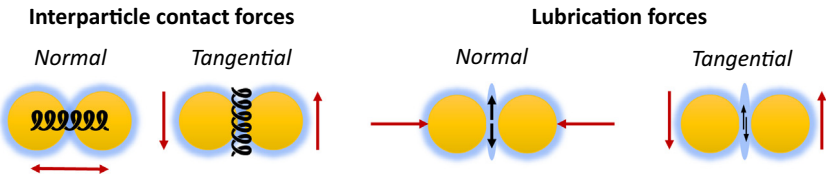


Fig. 2. Summary of contact forces acting on grinding media.

$$Y_{11}^C = 8\pi r_i^3 \left[\frac{2\beta}{5(1+\beta)} \ln\left(\frac{1}{\xi}\right) \right] \quad (10)$$

$$Y_{12}^C = 8\pi r_i^3 \left[\frac{\beta}{10(1+\beta)} \ln\left(\frac{1}{\xi}\right) \right] \quad (11)$$

where $\beta = r_j/r_i$, $\xi = 2h/(r_i + r_j)$ and h is the surface-surface separation. It is assumed that at high volume fraction, where interparticle gaps become very small compared to the particle size, the fluid in the gaps between particles can be considered laminar. At the same time, to reduce computational requirements, $F_i^{n,t}$ and $F_i^{t,t}$ are calculated for $0.001d_{ij} < h < 0.05d_{ij}$. It was previously verified that an outer cutoff of $0.1 \cdot d_{ij}$ does not give significantly different results [39]. The lower inner cutoff ($0.001 \cdot d_{ij}$) is chosen to reflect the asphericity/roughness of the beads' surfaces. Note that dissipative hydrodynamic lubrication forces acting prior to contact (i.e. with $h>0$) are distinct from the conventional dissipative terms used in damped DEM contacts. The latter are coupled to the presence of a contact, meaning repulsion and Coulombic friction are always present simultaneously with damping. The former constitute pairwise drag forces that can act at a distance and in the absence of repulsion and friction. During contact, the overall tangential force in our model comprises a static part (Eq. 4) and a dynamic part (Eq. 6).

These forces are derived for viscous flow [40] and they describe the squeezing and shearing of fluid in the narrow gaps between beads. Given the thinness of films over which they are calculated, and the dependence on relative pairwise velocity as opposed to absolute bead velocities, it is likely that the flow in these films remains viscous even under rapid milling [23,39]. Nonetheless, the model has also proven effective in describing the crossover from viscous to inertial flows of dense suspensions [17,20], so its use is not limited to laminar flows. Whereas frictional forces are calculated for particles in direct contact, lubrication forces are computed for particles separated by thin films. In the sections below, fluid viscosity $\eta_{f,i}$ is systematically varied to demonstrate the role of hydrodynamic lubrication in setting the overall milling power. It is reiterated here that we do not simulate milling itself, but rather systematically explore the behaviour at a range of fluid viscosities.

Rolling friction models are commonly used in DEM to reproduce the effect of particle shape or surface inhomogeneities [41,42]. In the case of ZrSiO₄ beads, a sintered structure designed for ultrafine grinding, with a very smooth surface to remove asperities (a common cause of interbatch crossed-contamination, due to product adhesion [43]), the actual bead shape is close to be an ideal sphere. Thus, frictional components representing both bead-bead and bead-surface interactions are accounted for in the coefficient of sliding friction, calibrated for that purpose, and no rolling friction is required.

3.2. Simulation setup details

Table 2 summarises the simulation input parameters. The density of the beads has been experimentally obtained by helium pycnometry (ULTRAPYC 1200e, Quantachrome GmbH, Germany) and the diameter size distribution by Dynamic Image Analysis (Camsizer P4, Retsch Technology GmbH, Germany). The nominal size input 1.8–2.0 correspond with Q_{10} and Q_{90} thresholds of the cumulative PSD. A bibliographic value for the Poisson's ratio (ν) has been included in the simulations. The other input parameters are determined as in **Section 3.1**.

Fig. 3 shows the considered laboratory mill geometry being initialised with 128,000 beads of diameter 1.8 mm, giving a 1:1 representation of the experimental system. The central stirrer is rotated with fixed angular rotation frequency (ramping up from 1000 to 4000 rpm), while the torque on the stirrer and the outer wall are measured by summing the tangential forces acting at all bead-wall contacts. The torque first increases as flow is initiated, with steady states being reached after about 5–10 complete rotations, depending on the frequency. The calculated torque and the reported results in **Section 4** are averaged over the steady state periods.

3.3. Modelling data processing and visualisation

The effect of viscosity on the shearing processes and the degree of mobilisation within the milling chamber is derived using grinding bead contact statistics. Following the analytical procedure first introduced by Beinert et al., 4 main collision types are isolated [16] (**Fig. 4**):

- Impact: as a result of the translational relative velocity between two beads, an impact on the normal direction of impact can be established with

$$E_i = \frac{1}{2}m(\vec{v}_{n,rel})^2 \quad (12)$$

where m is the mass of an individual bead and $\vec{v}_{n,rel}$ is the relative translational normal velocity between two beads.

- Torsion: this is caused by the rotational relative velocity between two beads with the normal contact as rotation axis:

$$E_t = \frac{1}{5}mr^2(\vec{\omega}_{n,rel})^2 \quad (13)$$

where r is the bead radius and $\vec{\omega}_{n,rel}$ is the relative rotational normal velocity.

Table 2

Summary of input parameters considered at the DEM simulation.

Setup properties		Further bead properties	
Quantity	Value	Quantity	Value
Total void volume (V_v)	0.910 l	Young's modulus (E)	5 MPa
Total bead solid in the mill (V_b)	0.393 l	Poisson's ratio (ν)	0.45
Diameter of the beads (d_b)	1.8–2.0 mm	Coefficient of restitution (COR)	0.50
Density of the beads (ρ_b)	6000 kg/m ³	Coefficient of friction (μ_p) (after calibration, Section 4.1)	0.30
Total mass of the beads (M_b)	2176 g	Time step	0.05 μs

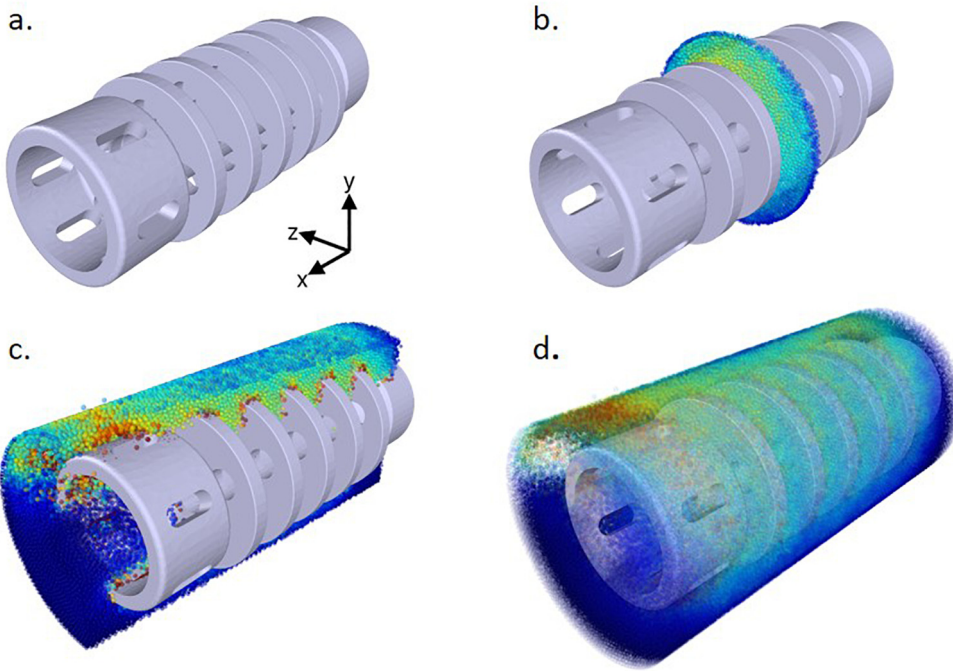


Fig. 3. DEM simulation screenshots of the inner section of the milling chamber. a. empty section showing stirrer; b. and c. internal view with cutting planes normal to x and z respectively; d. full section. Colours are used to provide a qualitative account of the velocity of the grinding beads.

- Shearing: this is an effect of the relative tangential velocity in the contact point. It can be caused by either the tangential velocity (Eq. 16) (Fig. 4, shearing a.), the rotational velocity (Eq. 17) (Fig. 4, shearing b.) or a combination of both (Fig. 4, shearing c.).

$$E_{s,t} = \frac{1}{2} m (\vec{v}_{s_1} - \vec{v}_{s_2})^2 \quad (14)$$

$$E_{s,r} = \frac{1}{5} m r^2 (\vec{\omega}_{s_1} - \vec{\omega}_{s_2})^2 \quad (15)$$

where \vec{v}_{s_i} is the shearing velocity and $\vec{\omega}_{s_i}$, the rotational counterpart, both extracted from the tangential component of velocity reduced by the rolling.

- Rolling: a result of the relative tangential velocity in the centre of contact between beads based on the translational and rotational velocity of both partners which act in the same direction (Fig. 4, rolling a., b. and c.).

$$E_{r,t} = \frac{1}{2} m (\vec{v}_{r_1} + \vec{v}_{r_2})^2 \quad (16)$$

$$E_{r,r} = \frac{1}{5} m r^2 (\vec{\omega}_{r_1} + \vec{\omega}_{r_2})^2 \quad (17)$$

where \vec{v}_{r_i} is the shearing velocity and $\vec{\omega}_{r_i}$, the rotational counterpart.

The different contact types do not occur in isolation, but rather with a combination of forms. The present study follows the analytical derivation of $\vec{v}_{n,rel}$, $\vec{\omega}_{n,rel}$, \vec{v}_{s_i} , $\vec{\omega}_{s_i}$, \vec{v}_{r_i} and $\vec{\omega}_{r_i}$ originally presented in [16]. A contact typology map is computed for 2 rotational velocities (1500 and 3500 rpm) at 5 different fluid viscosities ranging from 0.0 to 1.0 Pa.s.

Local profiles within the simulated mill are calculated by simple a coarse-graining approach (CG) that averages bead properties within spatial bins. This allows the calculation of continuum fields for properties by using the discrete outputs from DEM simulations. The main advantage of this technique is the ability to transform large sets of

microscopic data to represent the bulk behaviour of the granular material, along lines, planes or volumes of interest. Further details about this method and the definition of the spatial and temporal scales of the CG are provided elsewhere [44–46].

The velocity profile is determined as follows. First, it is assumed that each particle's mass is located at its centre r_i at time t . A macroscopic mass density field $\rho(r, t)$ can then be extracted with a coarse-graining function $\mathcal{W}(r)$, which leads to

$$\rho(r, t) = \sum_{i=1}^N m \mathcal{W}(r - r_i(t)) \quad (18)$$

A cut-off Gaussian coarse-graining function $\mathcal{W}(r)$ is given by.

$$\mathcal{W}(r) = V_\omega^{-1} \exp\left(-\frac{r^2}{2\omega^2}\right), \text{ if } r < c; \mathcal{W}(r) = V_\omega^{-1}, \text{ if } r > c \quad (19)$$

with a CG width $\omega_{CG} > 0$ and cut-off $c = 3\omega$. V_ω is a normalisation constant. The CG momentum density vector $p(r, t)$ can be extracted with

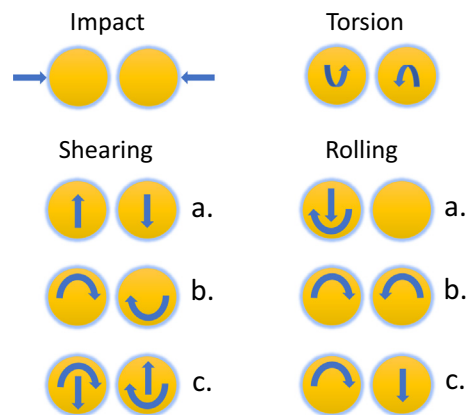


Fig. 4. Contact types and corresponding directions of translational and rotational velocities [16].

$$p(r, t) = \sum_{i=1}^N m v_i \mathcal{W}(r - r_i) \quad (20)$$

where v_i is the velocity of particle i . The macroscopic velocity field $V(r, t)$ is then defined as the ratio of momentum density and mass-related density field

$$V(r, t) = p(r, t)/\rho(r, t) \quad (21)$$

The results reported in Fig. 11 were averaged over a total of 106 snapshots, representing 52.5 ms of total simulation time, to generate 3D continuum fields of the grinding media velocity profile.

4. Results

4.1. Calibration of DEM parameters

Prior to establishing the effect of fluid viscosity ($\eta_{f,i}$), the bead-bead friction coefficient (μ_p) is calibrated against experimental tests. Taking as a benchmark experiment 1 (operation with dry beads without liquid), the simulation viscosity $\eta_{f,sim}$ is set to 0 and μ_p is systematically varied in the range 0.20 to 0.40 to extract the variation of P_i over a range of rotational speeds (ω) (Fig. 5.a). To determine the most appropriate value of μ_p , the square of the difference between the experimental power and the simulation prediction is summed for all the rotation frequencies (Fig. 5.b). A minimum is observed at $\mu_p=0.30$ and this value is used hereafter. Typical μ_p values of analogous analyses in

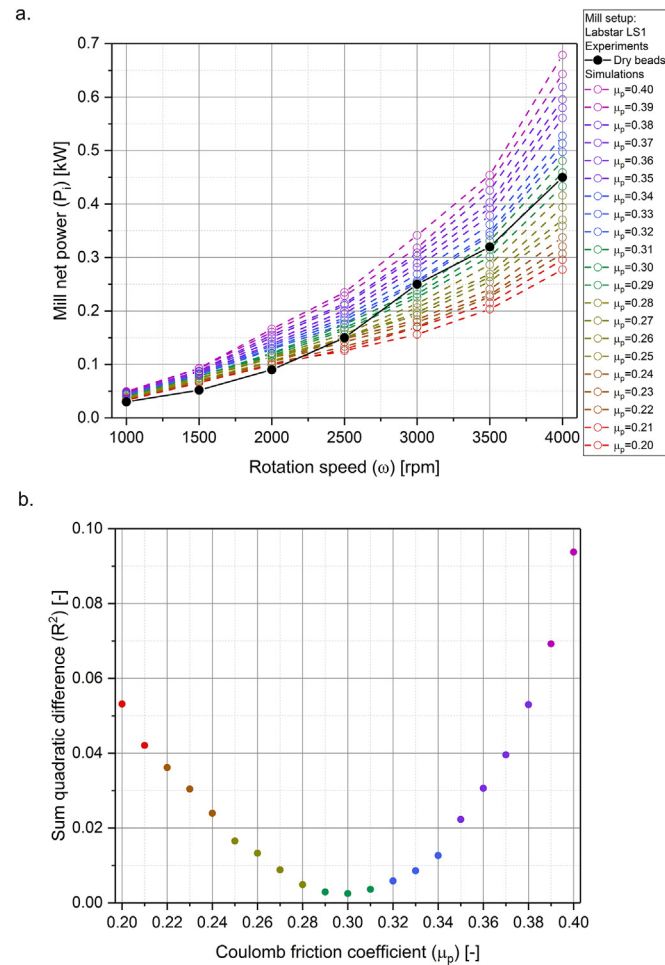


Fig. 5. a. DEM calibration of Coulomb friction coefficient (μ_p) vs dry experiments. b. Residuals of simulations vs. experiments.

DEM range from 0.20 to 0.40 for beads feeds of similar roughness and hardness [47,48]. μ_p is claimed to play two roles of a competitive nature in the flow: energy transfer and energy dissipation [36]. For high friction values, the dissipation mechanism is dominant so the kinetic energy decreases with increasing μ_p . Below the optimum value, the more energy is transferred between beads and faster the flow becomes. Recent experimental and numerical works have highlighted the crucial role of the friction coefficient in suspensions at high volume fraction [24,49,50]. In particular, it is understood that in suspensions with $\mu_p > 0$, the particle contact stress dominates over hydrodynamics at moderate-to-high volume fractions, adding support to our choice of numerical model.

The viscous dissipation between the grinding media and the interstitial fluid phase is defined by the simulation viscosity parameter $\eta_{f,sim}$. Importantly, this quantity is not precisely the viscosity of the suspending fluid since we are omitting long-range fluid effects, but it has the same dimensional units and performs the same physical role. Consequently, it is not expected that the choice of $\eta_{f,sim}$ should follow precisely that of $\eta_{f,exp}$. Instead, a DEM calibration methodology was applied by evaluating and comparing P_i of both experiments and simulations at a fixed rotation frequency. Fig. 6 reports P_i vs $\eta_{f,exp}$ for a series of water/glycerol mixtures of different relative compositions (Experiments 2–5), and the outputs (P_i vs $\eta_{f,sim}$) obtained from the respective DEM simulations. All tests were carried out at a constant speed of 2500 rpm.

4.2. Evaluation of the calibrated parameters

Fig. 7 presents a direct comparison, as function of increasing mill rotational speed and viscosity, between the DEM simulations and the experimental results. For each experiment the calibrated $\eta_{f,sim}$ was utilised. As it can be seen, the lubrication model is adequately capable of predicting P_i for a full range of operation rotation frequency and viscosities, with $\eta_{f,sim}$ having been calibrated only at 2500 rpm. The model tends to overestimate P_i at high rotation speeds and high viscosity. This can be attributed to the fact that the simulation operates at fixed temperature whereas the experimental temperature may increase slightly. Over the course of an experiment, with a rotation speed ramping up from 1000 to 4000 rpm, a typical temperature increase is 4 °C. This factor can lead to reductions in the fluid viscosity $\eta_{f,exp}$ of 0.08 Pa·s, thus accounting for the discrepancy in the results. At the same time, some

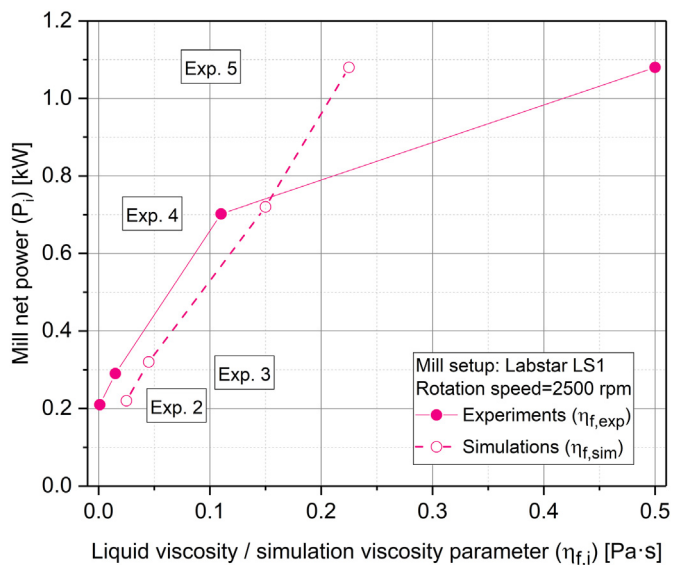


Fig. 6. Mill net power obtained from experiments and DEM simulations with varying liquid viscosity ($\eta_{f,i}$). Rotation speed: 2500 rpm.

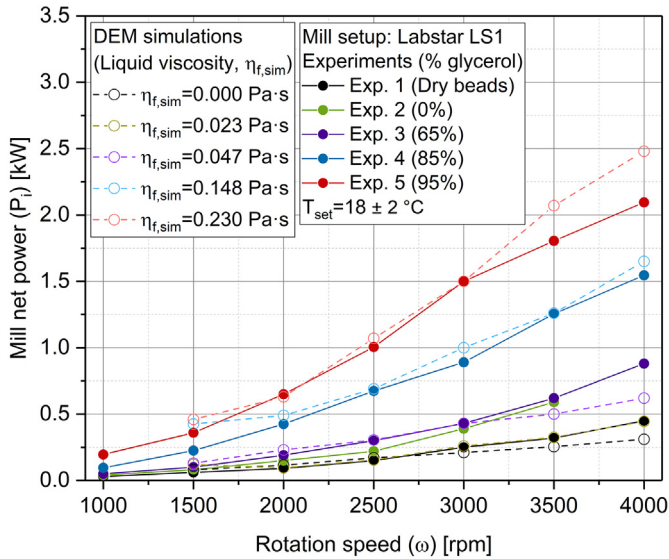


Fig. 7. Mill net power (P_i) obtained from experiments and DEM simulations with varying liquid viscosity (η_f).

fluctuations of the experimental P_i vs ω curve from 3000 rpm hints that the conveyed power by the motor is not linear.

4.3. Effect of viscosity on the dissipation of energy

Having established a set of model parameters that can match the experimental power curves over a broad range of rotation frequencies, the next step is to probe the internal dynamics of the mill. Below several examples are shown to illustrate aspects of the internal physics that may be interrogated with the model. The aim is not to give a comprehensive study here, but rather to demonstrate various kinds of physical insight that may be gained into specific milling process with this, or more sophisticated hydrodynamic lubrication models.

4.3.1. Energy dissipation maps

To evaluate the differences in energy dissipation modes and the local distribution of collisions along the mill chamber, the internal volume of the chamber is divided into 9 reference sections, identified with numbers from 1 to 3 and letters F, C, B, standing for front, centre and back, respectively (Fig. 8). All 9 regions would have identical volume if the mill chamber was an empty cylinder, but the presence of the stirrer perforated ceramic disk reduces the effective volume, especially for the innermost section (1).

Fig. 8 also accounts for the frequency of inter-bead collisions for η_f = 0.0; 0.5 and 1.0 Pa·s at ω = 1500 and 3500 rpm. A total of 10^6 timesteps, representing for ω = 1500 and 3500 rpm, 2 and 3 revolutions at steady state, respectively, are computed and the bead distribution at $t = 0$ s is homogeneous. Results are internally normalised and displayed in percent for a given η_f and ω with the aim to evaluate internal variation in the collision occurrence. The background colours are shared with the ones displayed in the legend to enhance readability.

The results demonstrate a significant gradient between the back part of the mill, closer to the motor, and the central and fore regions, where beads tend to flow due to their inertia at higher η_f (0.5 and 1.0 Pa·s). The maximum relative collision frequency difference can be identified between regions 1B and 3C at the test conditions with the least impeded bead mobility: highest ω (3500 rpm) with no lubrication forces acting on the bulk (2.1 vs 22.1%). No valuable analysis can be derived for an identical length dimension, but different radial location, as the inner radial region is mainly occupied by the ceramic disk.

4.3.2. Contact typologies

As described in Section 3.3 the energy dissipation spectrum is evaluated considering four inter-bead collision typologies: impact, torsion, shearing and rolling (Fig. 9). As it can be seen, highly energetic collision typologies (impact and torsion), mainly relying on free flows and inter-bead mobility, present a very minor occurrence. The most prominent contribution to the dissipation of energy in the system proceeds from the inter-particle forces acting tangentially as the system is highly packed and the mixing of beads cannot occur by cascading nor cataracting. Cascading and cataracting occur at high rates of rotation (for Froude numbers above 0.4) [51], when the height of the shear wedge rises above the bed surface and beads cascade or shower down on the free surface [52]. In the present scenario, as the system is highly packed, centrifugal forces impulse the grinding feed towards the lateral wall. Thus, around 98% of the total dissipation of energy takes place in the form of shearing or rolling. Shearing takes place by the friction caused by normal velocities acting in opposite directions, opposite rotational speeds or combinations of both. Normal interactions can dissipate a substantial amount of energy, but they require some extent of inter-bead mobility. Thus, the relative contribution of shearing decreases slightly when lubrication forces obstruct the flow of beads.

4.3.3. Dissipation modes

Fig. 10 provides a representation of the dissipated energy spectrum for the 9 reference regions across the mill for $\omega = 1500$. The occurrence of impact and torsion is only significant at the most external regions of the mill at low viscosities, where the presence of a small portion of free interstices between the bulk and the walls allows some beads to collide the external walls of the mill with a substantial rotational component. With decreasing viscosity, and thus reducing bead mobilisation, the translational energy becomes more dominant and thus the extent of impact and torsion energy dissipation. It has been claimed that rolling inter-bead contact contributions are negligible to product breakage [48,53]. That contribution to energy dissipation seems to be constant across regions and viscosities and thus not affecting the milling efficacy.

4.3.4. Coarse-grained velocities

The coarse-grained representation for the rotational and translational components of the velocity (Fig. 11) demonstrates two opposite tendencies for low and high viscosities. On one hand, for η_f = 0.0 Pa·s the rotational and translational velocity magnitudes present their maximum at the top-right section of the mill, coinciding with the maximum induced torque. On the other hand, for η_f = 1.0 Pa·s at the centre left region the velocity component is up to a factor of 5 larger than the right counterpart, fact attributed to tensile lubrication forces, damping and subsequent detachment linked with the viscous forces, at the region with the highest gravitational magnitude.

4.4. Discussion and future work

The simulation computational time is reported in Table 3 by computing the total elapsed time (wall-clock time). The variations in elapsed time for the same η_f are attributed to the heterogeneity of the cluster and not to an inherent variation of the physical phenomena occurring at different ω . Related CFD studies for milling applications are solved either for representative sections of the overall mill volume [16] or do not use the required grid resolution to capture interparticle fluid, which demand extended computations. The occurrence of hydrodynamic lubrication forces at small length scales requires a simulation cut-off of $0.001 \cdot d_{ij}$, that in an analogous analysis with a coupled methodology would lead to the definition of extraordinarily small simulation grids. Jayasundara et al. provided a CFD-DEM full reconstruction of a 201 IsaMill with a feed of 224,000 beads, but no information about the computational requirements was provided [54]. To the best of the authors knowledge, the total computation time of a classical CFD-DEM

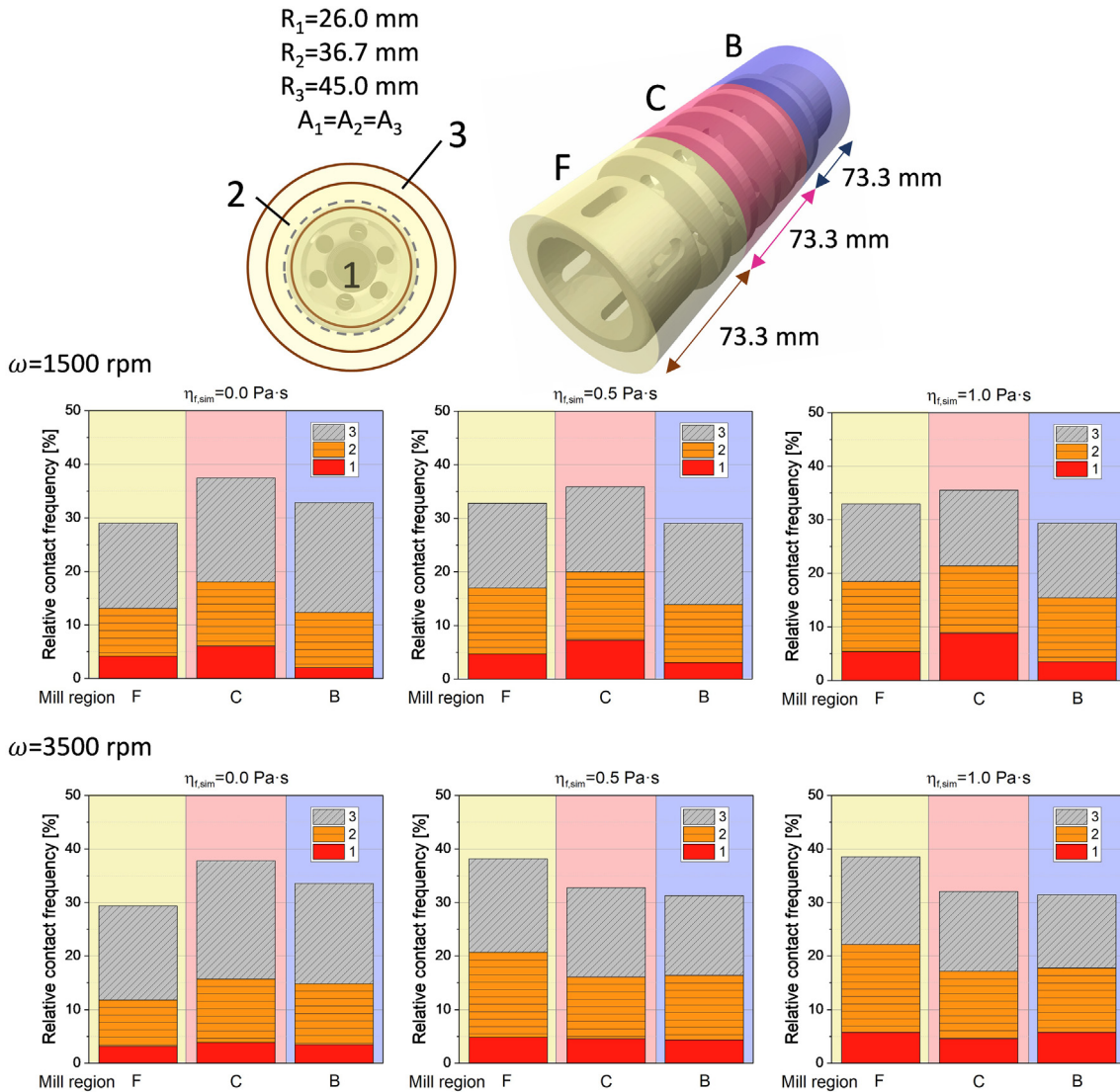


Fig. 8. (top) Legend of the abbreviations. F=front; C=centre; B=back. In discontinuous line, the cross section of the ceramic disk. (bottom) % Relative collision frequency internally normalised for each viscosity $\eta_{f,\text{sim}}=0.0; 0.5$ and $1.0\text{ Pa}\cdot\text{s}$, and rotation speed $\omega=1500$ and 3500 rpm .

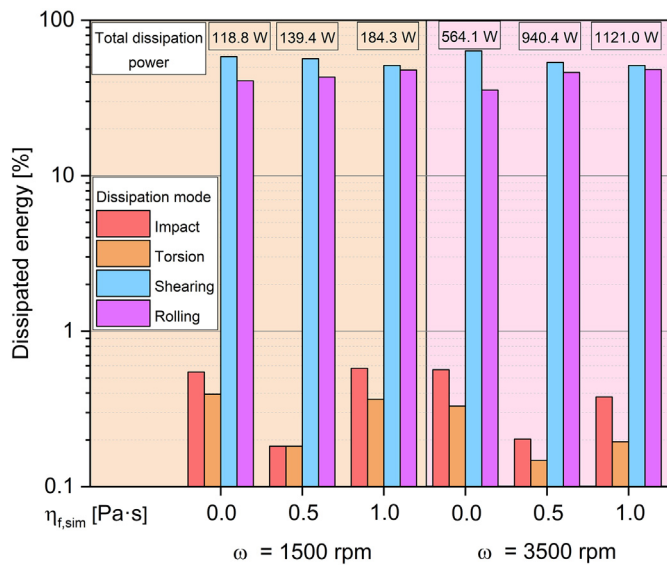


Fig. 9. % Dissipated energy per dissipation modes. $\omega=1500$ and 3500 rpm ; $\eta_{f,\text{sim}}=0.0, 0.5$ and $1.0\text{ Pa}\cdot\text{s}$. Labels indicate the total dissipated power in W.

modelling of a wet milling chamber has not been reported. However, Table 3 can be put into a wider context comparing the total elapsed time with fluidised systems. Amritkar et al. reported a CFD-DEM simulation of a fluidised bed with the solver MPI, taking into consideration 9240 particles with a total elapsed time around 2500 s, to compute 0.6 s of simulation [55]. The definition of an extremely large grid with a spacing of approximately 2.5 times the primary particle diameter and the reduced number of particles impedes any comparison with the current study. In the same line, another example of a CFD-DEM modelling of a fluidised bed with 25 million particles was carried out with a grid size of 1.74 times the primary diameter [56].

The present DEM modelling approach with the inclusion of hydrodynamic lubrication forces constitutes a good compromise between computational efficiency and an adequate description of the flow within the milling chamber. Future work will need to evaluate the application of this viscous lubrication model for high milling flow rates, different processing setups and filling media, and non-Newtonian interstitial fluids. The latter will clearly be a prerequisite for studying real milling applications in which the time-dependent rheology of the feed slurry is taken into account. As well as having fundamental value, knowledge of the rheology of slurries would be used as a direct input to DEM simulations of milling processes. In order to better understand milling efficiency, such simulations could address questions such as the milling

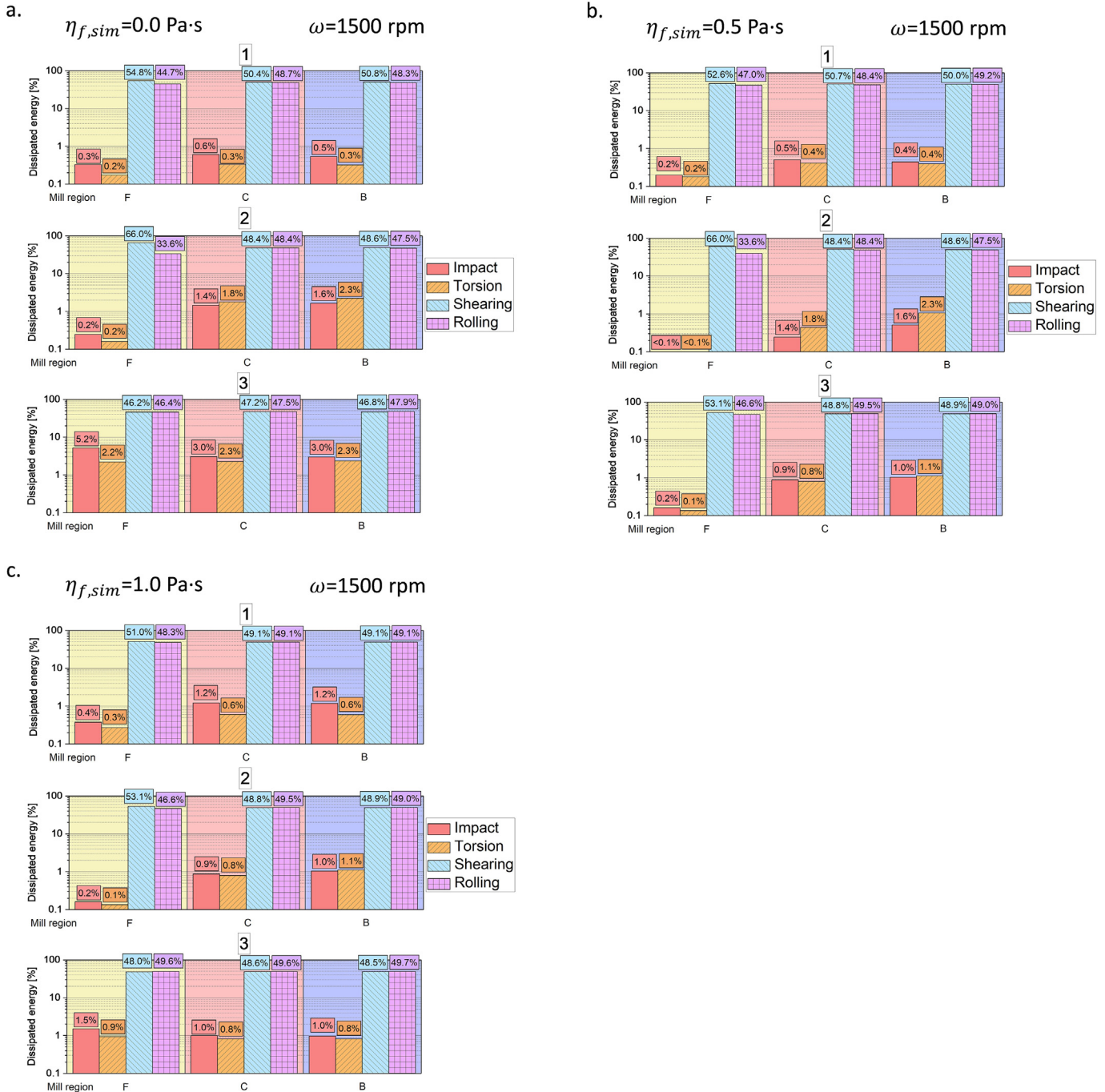


Fig. 10. % Dissipated energy per dissipation modes. $\omega = 1500$ rpm; a. $\eta_{f,sim}=0.0$; b. $\eta_{f,sim}=0.5$ and c. $\eta_{f,sim}=1.0 \text{ Pa}\cdot\text{s}$. Results displayed for 9 regions across the mill.

flow around the milling chamber, the collision direction and the role of friction. If product particles would be included in a coupled simulation, the exact description of every product-media contact would increase the quantitative characterisation and performance prediction of a mill.

Simulations with different hydrodynamic lubrication rheology – representing the dependency of the content of fines, for instance – add an additional level of complexity, and could be used to probe the evolution of bead behaviour as milling proceeds. The torque, residence time and power draw obtained from these simulations can be used to analyse the effect of different charges on the total product throughput. At the process level, population balances can be used to simulate the

evolution of the particle size distribution for wet milling operations. Stressing energy distributions can be extracted from the simulation and offer the possibility to calculate an overall effective collision frequency at certain process parameters. This material and machine dependent breakage rate can be correlated with the grinding process and be extended to dispersion processes.

5. Conclusions

A DEM simulation for a Netzsch Labstar mill at varying operation conditions is presented, in which the bead-bead interaction (representing

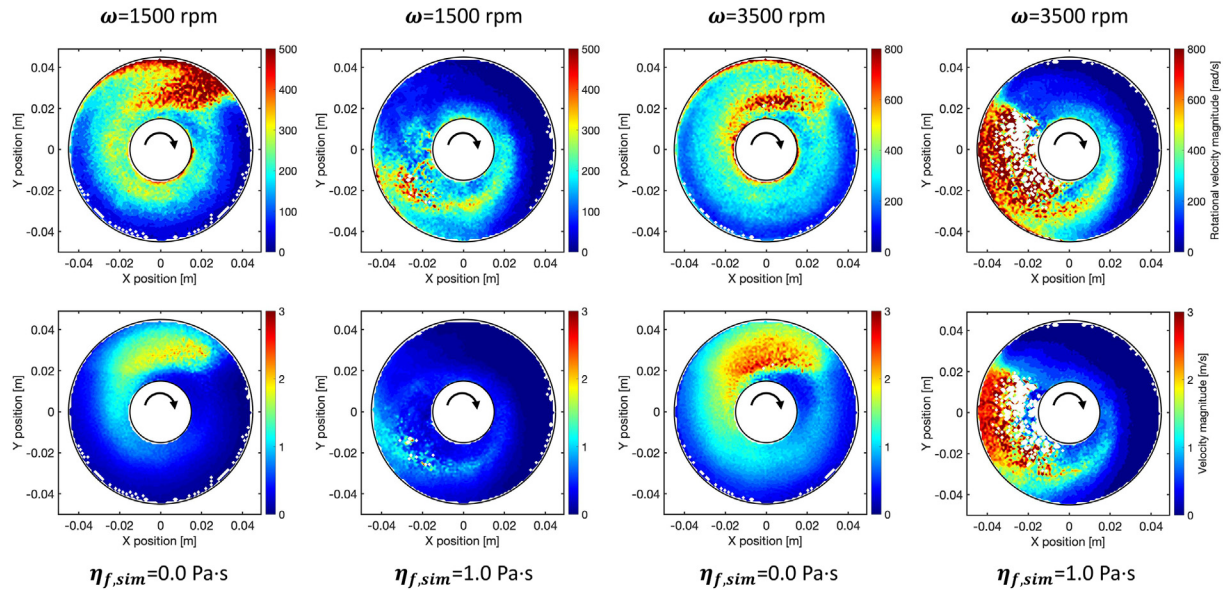


Fig. 11. Coarse grained profiles of rotational velocity magnitude and translational velocity magnitude. $\mu_p=0.3$; $\omega=1500$ and 3500 rpm; $\eta_{f,sim}=0.0$ and 1.0 Pa·s. Magnitudes averaged over a slice with of the mill between 96.5 and 108 mm in the X direction.

Table 3

Total elapsed simulation time for 52.5 ms of total simulation time. DEM simulations with lubrication forces with $\eta_{f,sim}=1.0$ Pa·s were run with 8 processors, whereas a single processor was used for $\eta_{f,sim}=0.0$ Pa·s.

ω [rpm]	Total elapsed time [h]	
	0.0	1.0
1000	44.2	21.2
1500	44.4	12.1
2000	42.4	31.2
2500	46.3	30.3
3000	44.8	38.6
3500	44.8	43.4
4000	45.0	35.6

collisions between grinding media beads) includes pairwise hydrodynamic lubrication in addition to frictional contact forces. The viscosity parameter in the lubrication forces represents the fluid phase, which in a typical application would be the feed slurry. The model accounts for multiphase effects in a simplified yet physically well-motivated way, circumventing the computational cost of a fully fluid-resolved model. Initially, a systematic calibration against experiments for the bead-bead friction coefficient (μ_p) and the simulation viscosity ($\eta_{f,sim}$) is carried out by varying the operating conditions: rotational speed and fluid viscosity. The simulation thereafter shows a good prediction for the empirical power draw across the full range of rotation frequencies and viscosities considered. The differences in energy dissipation modes and the local distribution of collisions along the mill chamber are examined for the extreme conditions of $\eta_{f,sim}=0$ Pa·s and $\eta_{f,sim}=1$ Pa·s. The most prominent contribution to the dissipation of energy in the system proceeds from the inter-particle forces acting tangentially (shearing and rolling). Highly energetic collision typologies (impact and torsion), mainly relying on free flows and inter-bead mobility, present a very minor occurrence. Finally, coarse-grained profiles of the velocities within the mill interior are presented, illustrating the detailed insight and the computational speed-up that may be gained with the model. Overall, the model presented here serves as a proof-of-concept to demonstrate that particle-based simulation may in principle offer a computationally tractable approach to simulating multiphase milling processes. This article has focussed on a simplified case in which the feed slurry is treated as

a Newtonian fluid both experimentally and computationally. Once the constitutive behaviour of real, practical, slurries is better known (a topic requiring further insights in future works), their rheology can be used to derive refined lubrication models that take into account phenomena such as shear thinning and thickening. Combining the latter with the model presented here is a promising route to new predictive models that can guide design and optimisation of wet milling.

List of abbreviations

CFD	Computational Fluid Dynamics
CG	Coarse Graining Analysis
DEM	Discrete Element Method
PEPT	Positron Emission Particle Tracking
PFEM	Particle Finite Element Method
SPH	Smooth Particle Hydrodynamics
VOF	Volume of Fluid

List of symbols and parameters

B	Mill bottom region [–]
C	Mill central region [–]
COR	Coefficient of restitution [–]
d_b	Diameter of the beads [mm]
E	Young's modulus [MPa]
E_i	Impact collision energy [J]
$E_{r,r}$	Rotational rolling collision energy [J]
$E_{r,t}$	Translational rolling collision energy [J]
$E_{s,r}$	Rotational sliding collision energy [J]
$E_{s,t}$	Translational sliding collision energy [J]
E_t	Torsional collision energy [J]
F	Mill forepart region [–]
$F_{ij}^{c,n}$	Normal repulsive contact force between particles i and j [N]
$F_{ij}^{c,t}$	Tangential repulsive contact force between particles i and j [N]
$F_{ij}^{l,n}$	Normal lubrication force [N]
h	Surface separation [m]
k_n	Normal stiffness constant [$N \cdot m^{-1}$]
k_t	Tangential stiffness constant [$N \cdot m^{-1}$]

I	Identity matrix [—]
M_b	Total mass of the bead charge [g]
m	Mass of a single bead [g]
n_{ij}	Centre-to-centre normal vector [—]
P_i	Experimental net power input [W]
P_{stat}	Stationary power draw [W]
P_0	No load or idle power [W]
$p(r,t)$	Coarsened-grained momentum density vector [$\text{kg} \cdot \text{m} \cdot \text{s}^{-1}$]
Q_i	Quantile cumulative distribution [—]
R_i	Mill cross-section radius [m]
r_i	Particle's radius [m]
u_{ij}^t	Elastic shear displacement [m]
V_b	Total bead solid in the mill [l]
V_v	Total void volume [l]
$V(r,t)$	Macroscopic velocity field [$\text{m} \cdot \text{s}^{-1}$]
V_ω	Coarse-graining normalisation constant [l]
v_i	Velocity [$\text{m} \cdot \text{s}^{-1}$]
v_{ij}	Relative interparticle velocity [$\text{m} \cdot \text{s}^{-1}$]
$\bar{v}_{n,rel}$	Relative normal translational velocity [$\text{m} \cdot \text{s}^{-1}$]
\bar{v}_{r_i}	Rolling velocity [$\text{m} \cdot \text{s}^{-1}$]
\bar{v}_{s_i}	Shearing velocity [$\text{m} \cdot \text{s}^{-1}$]
X_{11}^A	Lubrication force scalar resistance [m]
Y_{11}^A	Lubrication force scalar resistance [m]
Y_{21}^B	Lubrication force scalar resistance [m^2]
Y_{11}^C	Lubrication force scalar resistance [m^3]
Y_{12}^C	Lubrication force scalar resistance [m^3]
$\mathcal{W}(r)$	Coarse-graining function [—]
β	Radii ratio r_j/r_i [—]
γ_d	Normal damping coefficient [$\text{kg} \cdot \text{s}^{-1}$]
δ_{ij}	Centre-to-centre displacement [m]
$\eta_{f, exp}$	Experimental dynamic viscosity values [$\text{Pa} \cdot \text{s}$]
$\eta_{f, i}$	Liquid viscosity parameter [$\text{Pa} \cdot \text{s}$]
$\eta_{f, sim}$	Dynamic viscosity simulation input [$\text{Pa} \cdot \text{s}$]
μ_p	Coulombic friction coefficient [—]
ν	Poisson's ratio [—]
ξ	Distance over radii ratio [—]
ρ_b	Density of the charge of beads [$\text{kg} \cdot \text{m}^{-3}$]
$\rho(r,t)$	Macroscopic mass density field [kg]
ω	Rotation frequency [s^{-1}]
ω_{CG}	Coarse graining width [m]
ω_i	Angular velocity [s^{-1}]
$\dot{\omega}_{n,rel}$	Relative angular velocity [s^{-1}]
$\dot{\omega}_{r_i}$	Angular rolling velocity [s^{-1}]
$\dot{\omega}_{s_i}$	Angular shearing velocity [s^{-1}]

CRediT authorship contribution statement

Ramon Cabisco: Data curation, Visualization, Investigation, Formal analysis, Writing – original draft. **Tom Jansen:** Investigation, Formal analysis. **Michele Marigo:** Conceptualization, Formal analysis, Supervision. **Christopher Ness:** Conceptualization, Methodology, Formal analysis, Project Administration, Writing – review & editing.

Declaration of Competing Interest

The authors declare that they have no known competing financial interests or personal relationships that could have appeared to influence the work reported in this paper.

Acknowledgement

We thank Zilin Yan for useful discussions and technical support. CN was funded by the EPSRC and Johnson Matthey through a CASE

Studentship Award and latterly by the Royal Academy of Engineering through the Research Fellowship Scheme. An implementation of the lubrication forces described above is available at: doi:10.17863/CAM.13415.

References

- [1] A. Kwade, J. Schwedes, Wet grinding in stirred media mills, *Handbook of Powder Technology*, 12, 2007, pp. 251–382.
- [2] Y.-T. Hung, L.K. Wang, N.K. Shamma, *Handbook of Environment and Waste Management: Air and Water Pollution Control*, World Scientific, 2012.
- [3] M. Sinnott, P.W. Cleary, R. Morrison, Analysis of stirred mill performance using DEM simulation: part 1–media motion, energy consumption and collisional environment, *Miner. Eng. Min. Eng.* 19 (2006) 1537–1550.
- [4] H. Rumpf, Die Einzelkornzerkleinerung als Grundlage einer technischen Zerkleinerungswissenschaft, *Chemie Ingenieur Technik* 37 (1965) 187–202.
- [5] D. Daraio, J. Villoria, A. Ingram, A. Alexiadis, E.H. Stitt, M. Marigo, Investigating grinding media dynamics inside a vertical stirred mill using the discrete element method: effect of impeller arm length, *Powder Technol.* 364 (2020) 1049–1061, <https://doi.org/10.1016/j.powtec.2019.09.038>.
- [6] A. Strobel, B. König, S. Romeis, F. Schott, K.-E. Wirth, W. Peukert, Assessing stress conditions and impact velocities in fluidized bed opposed jet mills, *Particuology* 53 (December 2020) 12–22.
- [7] J. Tomas, T. Gröger, Mehrstufige turbulente Aerosortierung von Bauschutt, *AT. Aufbereitungs-Technik* 40 (1999) (1990) 379–386.
- [8] D. Schons, A. Kwade, Determination of the axial grinding media distribution in the IsaMill using radiometric densitometry, *Miner. Eng. Min. Eng.* 130 (2019) 110–116.
- [9] D. Daraio, J. Villoria, A. Ingram, A. Alexiadis, E. Hugh Stitt, M. Marigo, Validation of a discrete element method (DEM) model of the grinding media dynamics within an Attritor mill using positron emission particle tracking (PEPT) measurements, *Appl. Sci.* 9 (2019) 4816.
- [10] N.S. Weerasekara, M.S. Powell, P.W. Cleary, L.M. Tavares, M. Evertsson, R.D. Morrison, J. Quist, R.M. Carvalho, The contribution of DEM to the science of comminution, *Powder Technol.* 248 (2013) 3–24.
- [11] P.W. Cleary, DEM prediction of industrial and geophysical particle flows, *Particuology* 8 (2010) 106–118.
- [12] M.S. Powell, I. Govender, A.T. McBride, Applying DEM outputs to the unified comminution model, *Miner. Eng. Min. Eng.* 21 (2008) 744–750.
- [13] N. Metta, M. Ierapetritou, R. Ramachandran, A multiscale DEM-PBM approach for a continuous commilling process using a mechanistically developed breakage kernel, *Chem. Eng. Sci.* 178 (2018) 211–221, <https://doi.org/10.1016/j.ces.2017.12.016>.
- [14] R. Cabisco, J.H. Finke, A. Kwade, Assessment of particle rearrangement and anisotropy in high-load tabletting with a DEM-based elasto-plastic cohesive model, *Granul. Matter* 21 (2019) 98.
- [15] S. Larsson, B.I. Pålsson, M. Parian, P. Jonsén, A novel approach for modelling of physical interactions between slurry, grinding media and mill structure in wet stirred media mills, *Miner. Eng. Min. Eng.* 148 (2020) 106180.
- [16] S. Beinert, G. Fragnière, C. Schilde, A. Kwade, Analysis and modelling of bead contacts in wet-operating stirred media and planetary ball mills with CFD-DEM simulations, *Chem. Eng. Sci.* 134 (2015) 648–662.
- [17] D. Gao, J.A. Herbst, Alternative ways of coupling particle behaviour with fluid dynamics in mineral processing, *Int. J. Comput. Fluid Dynamics* 23 (2009) 109–118.
- [18] D. Gao, N.B. Morley, V. Dhir, Numerical simulation of wavy falling film flow using VOF method, *J. Comput. Phys.* 192 (2003) 624–642.
- [19] H.W. Graham, Smooth Particle Applied Mechanics: The State of the Art, World Scientific, 2006.
- [20] D. Violeau, B.D. Rogers, Smoothed particle hydrodynamics (SPH) for free-surface flows: past, present and future, *J. Hydraul. Res.* 54 (2016) 1–26.
- [21] F. Boyer, É. Guazzelli, O. Pouliquen, Unifying suspension and granular rheology, *Phys. Rev. Lett.* 107 (2011) 188301.
- [22] O. Cheal, C. Ness, Rheology of dense granular suspensions under extensional flow, *J. Rheol.* 62 (2018) 501–512.
- [23] M. Trulsson, B. Andreotti, P. Claudin, Transition from the viscous to inertial regime in dense suspensions, *Phys. Rev. Lett.* 109 (2012) 118305.
- [24] R. Seto, R. Mari, J.F. Morris, M.M. Denn, Discontinuous shear thickening of frictional hard-sphere suspensions, *Phys. Rev. Lett.* 111 (2013) 218301.
- [25] C. Ness, J.Y. Ooi, J. Sun, M. Marigo, P. McGuire, H. Xu, H. Stitt, Linking particle properties to dense suspension extrusion flow characteristics using discrete element simulations, *AICHE J.* 63 (2017) 3069–3082.
- [26] C. Ness, Z. Xing, E. Eiser, Oscillatory rheology of dense, athermal suspensions of nearly hard spheres below the jamming point, *Soft Matter Soft Matter*. 13 (2017) 3664–3674.
- [27] R.I. Tanner, C. Ness, A. Mahmud, S. Dai, J. Moon, A bootstrap mechanism for non-colloidal suspension viscosity, *Rheol. Acta* 57 (2018) 635–643.
- [28] E. Blanco, D.J. Hodgson, M. Hermes, R. Besseling, G.L. Hunter, P.M. Chaikin, M.E. Cates, I. Van Damme, W.C. Poon, Conching chocolate is a prototypical transition from frictionally jammed solid to flowable suspension with maximal solid content, *Proc. Natl. Acad. Sci.* 116 (2019) 10303–10308.
- [29] J.J.J. Gillissen, C. Ness, J.D. Peterson, H.J. Wilson, M.E. Cates, Constitutive model for shear-thickening suspensions: predictions for steady shear with superposed transverse oscillations, *J. Rheol.* 64 (2020) 353–365.
- [30] S. Breitung-Faes, A. Kwade, Use of an enhanced stress model for the optimization of wet stirred media milling processes, *Chem. Eng. Technol.* 37 (2014) 819–826.

- [31] FOX Industries, Zirconium Silicate – Grinding Media for Your Bead Mill, <http://foxindustries.com/products/grinding-media/zirconium-silicate-grinding-beads/> 2019. (Accessed 19 July 2020).
- [32] Y.M. Chen, A.J. Pearlstein, Viscosity-temperature correlation for glycerol-water solutions, *Ind. Eng. Chem. Res.* 26 (1987) 1670–1672.
- [33] A. Volk, C.J. Kähler, Density model for aqueous glycerol solutions, *Exp. Fluids* 59 (2018) 75.
- [34] C. Kloss, C. Goniva, LIGGGHTS—open source discrete element simulations of granular materials based on LAMMPS, *Supplemental Proceedings: Materials Fabrication, Properties, Characterization, and Modeling*, 2, 2011, pp. 781–788.
- [35] P.A. Cundall, O.D. Strack, A discrete numerical model for granular assemblies, *Geotechnique*, 29 (1979) 47–65.
- [36] R.Y. Yang, C.T. Jayasundara, A.B. Yu, D. Curry, DEM simulation of the flow of grinding media in IsaMill, *Miner. Eng. Min. Eng.* 19 (2006) 984–994.
- [37] P.Y. Liu, R.Y. Yang, A.B. Yu, DEM study of the transverse mixing of wet particles in rotating drums, *Chem. Eng. Sci.* 86 (2013) 99–107.
- [38] M.V. Machado, D.A. Santos, M.A. Barrozo, C.R. Duarte, Experimental and numerical study of grinding media flow in a ball mill, *Chem. Eng. Technol.* 40 (2017) 1835–1843.
- [39] C. Ness, J. Sun, Flow regime transitions in dense non-Brownian suspensions: rheology, microstructural characterization, and constitutive modeling, *Phys. Rev. E* 91 (2015), 012201..
- [40] S. Kim, S.J. Karrila, *Microhydrodynamics* Butterworth, Heinemann, Boston, 1991.
- [41] C.M. Wensrich, A. Katterfeld, Rolling friction as a technique for modelling particle shape in DEM, *Powder Technol.* 217 (2012) 409–417.
- [42] A. Singh, C. Ness, R. Seto, J.J. de Pablo, H.M. Jaeger, Shear thickening and jamming of dense suspensions: the “roll” of friction, *Phys. Rev. Lett.* 124 (2020) 248005.
- [43] A.R. Jones, Mechanical alloying, in: K.H.J. Buschow, R.W. Cahn, M.C. Flemings, B. Ilschner, E.J. Kramer, S. Mahajan, P. Veyssiére (Eds.), *Encyclopedia of Materials: Science and Technology*, Elsevier, Oxford 2001, pp. 1–5, <https://doi.org/10.1016/B0-08-043152-6/00912-8>.
- [44] M. Babic, Average balance equations for granular materials, *Int. J. Eng. Sci.* 35 (1997) 523–548.
- [45] I. Goldhirsch, Stress, stress asymmetry and couple stress: from discrete particles to continuous fields, *Granul. Matter* 12 (2010) 239–252.
- [46] T. Weinhart, C. Labra, S. Luding, J.Y. Ooi, Influence of coarse-graining parameters on the analysis of DEM simulations of silo flow, *Powder Technol.* 293 (2016) 138–148.
- [47] M. Khanal, C.T. Jayasundara, Role of particle stiffness and inter-particle sliding friction in milling of particles, *Particuology* 16 (2014) 54–59.
- [48] S. Beinert, G. Fragnière, C. Schilde, A. Kwade, Multiscale simulation of fine grinding and dispersing processes: stressing probability, stressing energy and resultant breakage rate, *Adv. Powder Technol.* 29 (2018) 573–583.
- [49] C. Ness, J. Sun, Shear thickening regimes of dense non-Brownian suspensions, *Soft Matter Soft Matter*. 12 (2016) 914–924.
- [50] J. Comtet, G. Chatté, A. Niguès, L. Bocquet, A. Siria, A. Colin, Pairwise frictional profile between particles determines discontinuous shear thickening transition in non-colloidal suspensions, *Nat. Commun.* 8 (2017) 1–7.
- [51] H. Henein, Experimental study of transverse bed motion in rotary kilns, *Mater. Mater. Trans. B* 14 (1983) 15.
- [52] A.A. Boateng, *Rotary Kilns: Transport Phenomena and Transport Processes*, Elsevier/Butterworth-Heinemann, 2008.
- [53] G. Fragnière, S. Beinert, A. Overbeck, I. Kampen, C. Schilde, A. Kwade, Predicting effects of operating condition variations on breakage rates in stirred media mills, *Chem. Eng. Res. Des.* 138 (2018) 433–443.
- [54] C.T. Jayasundara, R.Y. Yang, B.Y. Guo, A.B. Yu, I. Govender, A. Mainza, A. van der Westhuizen, J. Rubenstein, CFD-DEM modelling of particle flow in IsaMills—comparison between simulations and PEPT measurements, *Miner. Eng. Min. Eng.* 24 (2011) 181–187.
- [55] A. Amritkar, S. Deb, D. Tafti, Efficient parallel CFD-DEM simulations using OpenMP, *J. Comput. Phys.* 256 (2014) 501–519.
- [56] D. Jajcevic, E. Siegmann, C. Radeke, J.G. Khinast, Large-scale CFD-DEM simulations of fluidized granular systems, *Chem. Eng. Sci.* 98 (2013) 298–310, <https://doi.org/10.1016/j.ces.2013.05.014>.